Motion-compensated diffusion encoding in multi-shot human brain acquisitions: Insights using high-performance gradients

Journal Article

Author(s):
Michael, Eric Seth; Hennel, Franciszek; Pruessmann, Klaas Paul

Publication date:
2024

Permanent link:
https://doi.org/10.3929/ethz-b-000664621

Rights / license:
Creative Commons Attribution-NonCommercial 4.0 International

Originally published in:
Magnetic Resonance in Medicine, https://doi.org/10.1002/mrm.30069

Received: 13 September 2023 | Revised: 12 December 2023 | Accepted: 9 February 2024
DOI: 10.1002/mrm.30069

RESEARCH ARTICLE

Magnetic Resonance in Medicine

Motion-compensated diffusion encoding in multi-shot human brain acquisitions: Insights using high-performance gradients

Eric Seth Michael | **Franciszek Hennel** | **Klaas Paul Pruessmann**

Institute for Biomedical Engineering,
ETH Zurich and University of Zurich,
Zurich, Switzerland

Correspondence
Eric Seth Michael, Institute for Biomedical Engineering, ETH Zurich and University of Zurich, Gloriastrasse 35, 8092 Zurich, Switzerland.
Email: michael@biomed.ee.ethz.ch

Abstract

Purpose: To evaluate the utility of up to second-order motion-compensated diffusion encoding in multi-shot human brain acquisitions.

Methods: Experiments were performed with high-performance gradients using three forms of diffusion encoding motion-compensated through different orders: conventional zeroth-order–compensated pulsed gradients (PG), first-order–compensated gradients (MC1), and second-order–compensated gradients (MC2). Single-shot acquisitions were conducted to correlate the order of motion compensation with resultant phase variability. Then, multi-shot acquisitions were performed at varying interleaving factors. Multi-shot images were reconstructed using three levels of shot-to-shot phase correction: no correction, channel-wise phase correction based on FID navigation, and correction based on explicit phase mapping (MUSE).

Results: In single-shot acquisitions, MC2 diffusion encoding most effectively suppressed phase variability and sensitivity to brain pulsation, yielding residual variations of about 10° and of low spatial order. Consequently, multi-shot MC2 images were largely satisfactory without phase correction and consistently improved with the navigator correction, which yielded repeatable high-quality images; contrarily, PG and MC1 images were inadequately corrected using the navigator approach. With respect to MUSE reconstructions, the MC2 navigator-corrected images were in close agreement for a standard interleaving factor and considerably more reliable for higher interleaving factors, for which MUSE images were corrupted. Finally, owing to the advanced gradient hardware, the relative SNR penalty of motion-compensated diffusion sensitization was substantially more tolerable than that faced previously.

Conclusion: Second-order motion-compensated diffusion encoding mitigates and simplifies shot-to-shot phase variability in the human brain, rendering the multi-shot acquisition strategy an effective means to circumvent limitations of retrospective phase correction methods.

KEYWORDS
diffusion-weighted imaging, motion compensation, multi-shot DWI, navigator, phase correction

1 INTRODUCTION

Diffusion-weighted (DW) MRI acquisitions are typically performed using single-shot readouts, but the attainable spatial resolution is practically limited by T_2* blurring and off-resonance artifacts,[1] which worsen with a prolonged acquisition window. Multi-shot acquisitions, on the other hand, are desirable because segmentation of the spatial encoding window into shorter snippets curbs T_2* and off-resonance issues, permitting higher achievable resolution; however, interleaved diffusion acquisitions (i.e., those with diffusion encoding performed for each acquisition interval) incur the necessity to correct for phase variations between shots. Shot-to-shot phase inconsistencies occur because conventional Stejskal-Tanner diffusion encodings[2] have uncompensated first- and higher-order moments that cause phase accrual for equivalent-order subject motion (e.g., bulk involuntary movement, cardiac pulsation, respiration) during diffusion sensitization, and such motion[3] varies across shots.

Much research effort has been devoted to the development of reconstruction methods that retrospectively correct for shot-to-shot phase differences in multi-shot diffusion imaging.[4] Correction strategies initially relied on the acquisition of additional navigators[5] to estimate phase differences across interleaves.[6–10] Later, explicit phase-mapping approaches were developed, in which either the k-space center was oversampled to reconstruct low-resolution images per shot,[11,12] or parallel imaging[13,14] was used to directly reconstruct images for individual shots;[15,16] in both cases, per-shot phase maps could be obtained and fed into a reconstruction over all shots. The performance of these explicit phase-mapping methods was subsequently improved by iteratively updating the derived phase estimates.[17–20] More recently, low-rank reconstruction algorithms[21–23] were proposed to bypass the explicit phase estimation step, providing better robustness with respect to explicit phase mapping at higher interleaf factors.[24] Additionally, reconstruction models incorporating macroscopic motion between interleaves were developed,[25–28] as well as strategies for multi-slice diffusion acquisitions.[24,29–31] A drawback of these increasingly complex reconstruction strategies is that the assumed or enforced smoothness of motion-induced phase inherently restricts attainable image accuracy, especially at higher interleaf factors for which undersampling impedes the estimation or inference of phase in each shot. A further disadvantage of these methods is computation time, which limits their use.[32,33]

An alternative means of combatting phase variability in multi-shot diffusion experiments is to eliminate the cause of shot-to-shot phase differences, that is, to null the moments of the diffusion encoding gradients. Diffusion gradient shapes with nulled higher-order moments incur no phase accrual for equivalent-order time derivatives of motion, thereby reducing shot-to-shot phase differences, but encode diffusion less efficiently and require longer TEs (for a given b-value), thereby reducing SNR. Motion-compensated diffusion encoding is commonly employed in cardiac[34–36] and abdominal organ diffusion imaging,[37–39] in which severe physiological motion necessitates such encoding to avoid irreversible intravoxel dephasing, even in single-shot acquisitions. The strategy was also shown to mitigate artifacts in single-shot diffusion-prepared brain acquisitions with extreme, continuous motion (up to 20° rotation).[40] Even in the absence of large head movements, the prospect of suppressed phase variability renders motion-compensated diffusion encoding attractive for multi-shot acquisitions. The use of first-order–compensated diffusion sensitization in multi-shot brain acquisitions was adopted[41–44] during the early stages of the aforementioned advances in reconstruction strategy—roughly coinciding with the development of the initial navigator-based approaches—and resulted in artifact reduction (albeit with residual ghosting); however, the relative diffusion-encoding inefficiency incurred by moment-nulling at contemporary gradient strengths (up to about 20 mT/m) was a significant disadvantage.[3] To our knowledge, the strategy has since been practically abandoned in multi-shot in vivo human brain imaging in favor of the proliferating retrospective phase correction methods, likely due to the substantial SNR penalty of motion compensation.

Over the same time span, gradient technology has continually improved, leading to steadily increasing gradient strengths and a recent advent of high-performance gradient systems,[45–49] which are about an order of magnitude stronger than those at the time of previous multi-shot, motion-compensated diffusion experiments. As a result, the relative TE burden and consequent SNR disadvantage of less-efficient diffusion gradient shapes have greatly reduced, thereby abating the practical limitations of using motion-compensated diffusion gradients in multi-shot acquisitions and warranting a reconsideration of the strategy. To this end, in this work we evaluate the utility of up to second-order motion-compensated diffusion sensitization in multi-shot DWI of the in vivo human brain using a high-performance gradient system.[46] We first establish the phase variability resulting from diffusion encoding with different orders of motion compensation in repeated single-shot acquisitions. Subsequently, we utilize these diffusion encodings in multi-shot acquisitions with varying interleaving factors and for varying degrees of correction for shot-to-shot phase variability in image reconstruction, for which a conventional reconstruction procedure based

TABLE 1 Experimental parameters for Experiments 1–3.

	Diffusion gradients	Shots	Readout	TE (ms)	In-plane resolution (mm)	Repetitions
Experiment 1	PG	1	Spiral	23	2	15
	MC1	1	Spiral	38	2	15
	MC2	1	Spiral	41	2	15
Experiment 2	PG	3	Spiral	23	1	4
		3	EPI	45	1.5	4
	MC1	3	Spiral	38	1	4
		3	EPI	65	1.5	4
	MC2	3	Spiral	41	1	4
		3	EPI	68	1.5	4
Experiment 3	PG	6, 8, 10	Spiral	23	1	2 (10-shot) 3 (others)
		5, 7	EPI	52 (5-shot) 42 (7-shot)	1	3
	MC2	6, 8, 10	Spiral	41	1	2 (10-shot) 3 (others)
		5, 7	EPI	75 (5-shot) 64 (7-shot)	1	3

Abbreviations: MC1, first-order–compensated bipolar gradients; MC2, second-order–compensated bipolar gradients; PG, zeroth-order–compensated pulsed gradients.

on explicit phase mapping (i.e., MUSE)[15] served as a standard for comparison.

2 | METHODS

2.1 | Data acquisition

Imaging experiments were carried out using a Philips 3T Achieva system (Philips Healthcare, Best, the Netherlands) equipped with a high-performance gradient insert coil[46] reaching $G_{max} = 200$ mT/m and $SR_{max} = 600$ mT/m/ms at 100% duty cycle and an eight-channel RF transmit-receive array coil[50] that was custom-built for neuroimaging with the gradient system.

The impact of different orders of motion compensation in diffusion encoding was evaluated over three experiments, which are explained in the following sections (see Table 1 for details). Two healthy adult males volunteered for participation in all experiments in accordance with applicable ethics policy. Over the experiments, three diffusion-sensitizing gradient waveforms were deployed, each motion-compensated through a different order: (1) conventional zeroth-order–compensated monopolar gradients (i.e., pulsed gradients, abbreviated PG),[2] (2) first-order–compensated bipolar gradients (MC1),[51] and (3) second-order–compensated bipolar gradients (MC2).[52] The gradient waveforms achieved a b-value of 1000 s/mm^2 using gradient amplitudes near the aforementioned specification while minimizing TE and are shown in Figure S1. The acquisitions in all experiments used three diffusion directions (along the Cartesian coordinate axes), 10 slices, FOV = 220 × 220 mm^2, slice thickness = 3 mm, slice gap = 2 mm, and TR = 4000 ms.

2.1.1 | Experiment 1

To assess phase variability over repeated acquisitions for each order of motion compensation, ten repetitions of single-shot spiral acquisitions (2-mm in-plane resolution) were performed for each diffusion gradient waveform (TE = 23, 38, and 41 ms for PG, MC1, and MC2, respectively).

2.1.2 | Experiment 2

To evaluate the utility of motion-compensated diffusion encoding in standard multi-shot acquisitions, three-shot acquisitions (four repetitions) were performed for each diffusion gradient waveform. Images were reconstructed using three levels of correction for shot-to-shot phase variability (see Section 2.2) to determine the adequacy of each correction for each order of compensation. Acquisitions were paired with both spiral and EPI[53] readouts (1-mm and 1.5-mm in-plane resolutions, respectively) to judge this performance against the imaging gradient trajectory. The spiral TEs were the same as in Experiment 1, and the EPI TEs were 45, 65, and 68 ms for PG, MC1, and MC2, respectively.

2.1.3 | Experiment 3

Finally, to examine the effect of motion compensation in more challenging multi-shot acquisitions—in particular, at interleaving factors for which conventional phase-mapping–based reconstruction struggles—highly interleaved acquisitions were performed using PG and MC2 diffusion encoding; spiral trajectories with 6, 8, and 10 shots and EPI trajectories with 5 and 7 shots were used (1-mm in-plane resolution for all cases). All acquisitions were repeated three times except for the 10-shot spiral acquisitions, which were repeated two times. Images were again reconstructed using three forms of correction for shot-to-shot phase variability to assess the adequacy of each level of correction. The spiral TEs were the same as in Experiment 1, and the EPI TEs were 52 ms and 75 ms for 5-shot acquisitions and 42 and 64 ms for 7-shot acquisitions for PG and MC2, respectively.

2.2 | Imaging gradient trajectories

All EPI and spiral trajectories were designed using an in-house pipeline that constructs the shortest possible gradient waveform for given gradient and slew rate limitations, G_{lim} and SR_{lim}, respectively. For the spiral trajectories, $G_{\mathrm{lim}} = 200$ mT/m and $SR_{\mathrm{lim}} = 600$ mT/m/ms were used, but for EPI trajectories $G_{\mathrm{lim}} = 40$ mT/m and $SR_{\mathrm{lim}} = 200$ mT/m/ms were used to mitigate ghosting induced by eddy currents.

2.3 | Image reconstruction

All acquisitions were repeated to monitor the spatiotemporal field dynamics during readout using a field camera based on ^{1}H NMR field probes[54] (Skope Magnetic Resonance Technologies, Zurich, Switzerland). Third-order spherical harmonic field models, which were corrected for second-order concomitant fields,[1] were fitted to these data and were used in combination with off-resonance maps in a higher-order algebraic reconstruction algorithm.[55]

The three forms of shot-to-shot phase correction implemented in Experiments 2 and 3 are schematically illustrated in Figure 1. The first and simplest scheme was a direct (i.e., "native") reconstruction over all interleaves, in which shot-to-shot phase differences were not corrected for.

The second strategy, which required negligible additional computation with respect to native reconstruction, entailed multiplication of MR signal of each shot by a phase factor[6] based on FID navigation[56] (i.e., momentary signal acquisition at $k = 0$ before readout). This navigator phase correction was performed channel-wise and is given by

$$s_{\gamma,\xi}^{\mathrm{img,corr}} = s_{\gamma,\xi}^{\mathrm{img}} e^{-i\varphi_{\gamma,\xi}^{\mathrm{nav}}} \tag{1}$$

where $s_{\gamma,\xi}^{\mathrm{img}}$ is the complex MR signal measured during the readout of interleaf ξ by channel γ, and $\varphi_{\gamma,\xi}^{\mathrm{nav}}$ is the phase of the phase factor for interleaf ξ and channel γ, given by

$$\varphi_{\gamma,\xi}^{\mathrm{nav}} = \mathrm{angle}\left(\overline{s_{\gamma,\xi}^{\mathrm{nav}}}\right), \tag{2}$$

where $s_{\gamma,\xi}^{\mathrm{nav}}$ is the complex MR signal measured at $k = 0$ before the readout of interleaf ξ by channel γ, and the bar denotes time averaging over the relevant k-space center sampling interval. To facilitate this strategy, the acquisitions of Experiments 2 and 3 included a 0.5-ms measurement at $k = 0$ before readout; only the final 100 acquisition samples (131 μs) before the imaging gradients were used to determine $\varphi_{\gamma,\xi}^{\mathrm{nav}}$.

The final phase correction strategy employed here utilized explicit per-shot phase maps, as in MUSE[15] and SENSE+CG;[16] the strategy is hereafter referred to as MUSE. This reconstruction was implemented as a two-step process: first, individual images were reconstructed for each shot using SENSE;[14] second, low-pass–filtered phase maps from the images computed in the first step were used in a reconstruction over all interleaves by incorporating the spatially varying per-shot phase into the encoding model. Using the matrix–vector encoding notation,[13] the encoding matrix E used in the higher-order reconstruction of the second step is given by

$$\mathrm{E}_{(\gamma,\kappa),\rho} = c_\gamma\left(\mathbf{r}_\rho\right) \times e^{i\left[\Delta\omega(\mathbf{r}_\rho)t_\kappa + \sum_l k_l(t_\kappa)b_l(\mathbf{r}_\rho) + \varphi^{(\mathrm{CF})}(t_\kappa,\mathbf{r}_\rho) + \varphi^{(\mathrm{MUSE})}(\xi_\kappa,\mathbf{r}_\rho)\right]}, \tag{3}$$

where c_γ denotes the complex sensitivity of the γth channel, $\mathbf{r}_\rho$ the position of the ρth pixel, $\Delta\omega$ the demodulated off-resonance frequency, t_κ the time since excitation of the κ-th signal sample, k_l the coefficient of the l-th spherical (solid) harmonic basis function b_l as determined by field monitoring, $\varphi^{(\mathrm{CF})}$ the phase evolution corresponding to concomitant fields (which were determined as described by Wilm et al.),[1] $\varphi^{(\mathrm{MUSE})}$ the per-shot phase associated with MUSE, and ξ_κ the interleaf number of the of the κ-th signal sample. The size of E is $N_\kappa N_\gamma \times N_\rho$, where N_κ, N_γ, and N_ρ are the numbers of samples, channels, and reconstructed

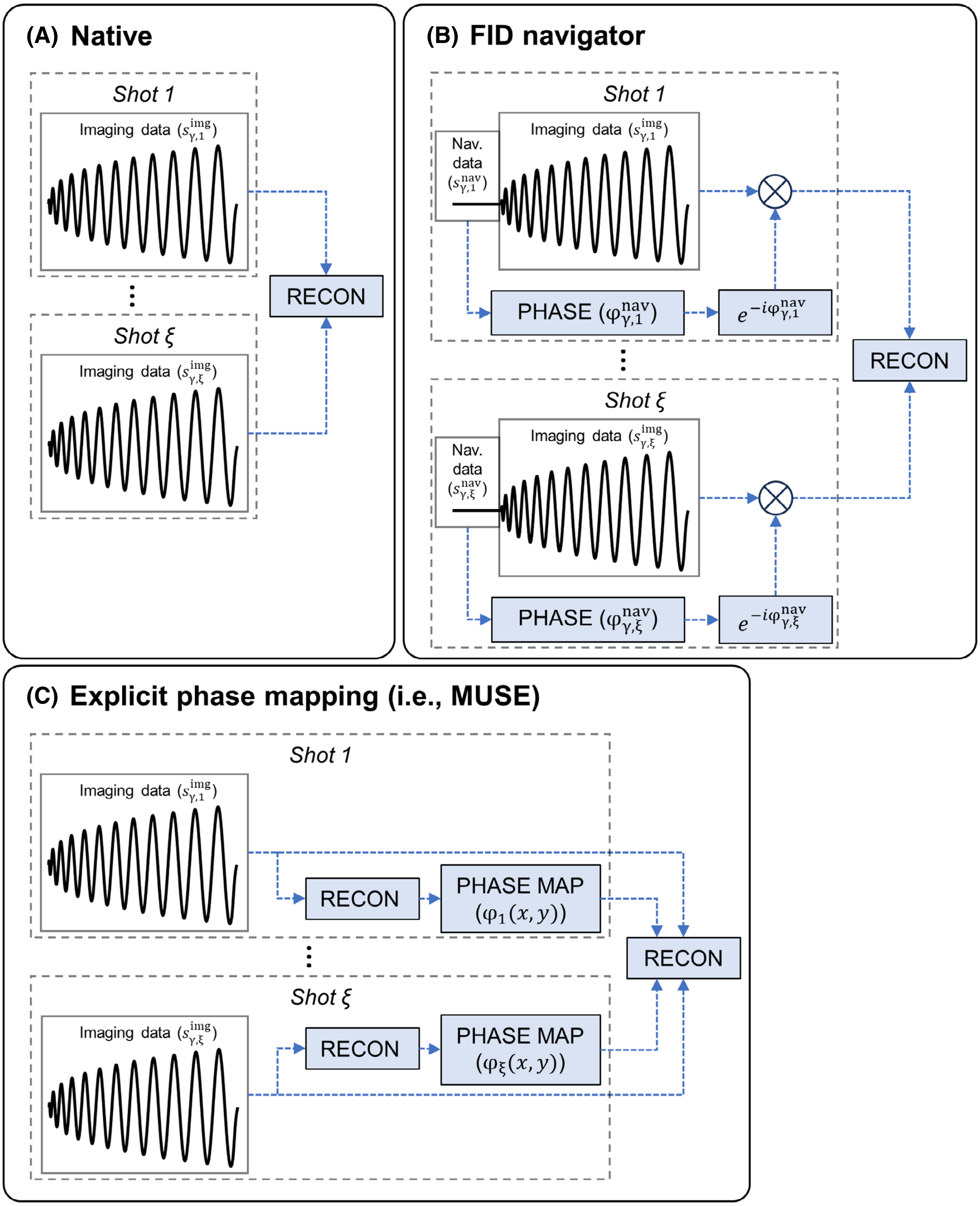

FIGURE 1 Schematic diagrams of reconstruction strategies for multi-shot diffusion data: native (A), FID navigator (B), and explicit phase mapping (C). The term "RECON" generically represents image reconstruction, which may include, for example, the conjugate gradient algorithm, the SENSE algorithm, B_0 off-resonance correction, and field monitoring data.

pixels, respectively, and interleaves are concatenated along N_κ (i.e., $N_\kappa = N_\xi N_{\breve{\kappa}}$ for a N_ξ-shot acquisition with $N_{\breve{\kappa}}$ signal samples per interleaf). It is noted that the addition of $\varphi^{(\text{MUSE})}$ to the exponential is equivalent to the use of composite sensitivity profiles.[11]

2.4 | Image preprocessing and analysis

All reconstructed images were corrected for Gibbs ringing[57] then bias field-corrected[58] using SPM12 (http://www.fil.ion.ucl.ac.uk/spm/software/spm12/).

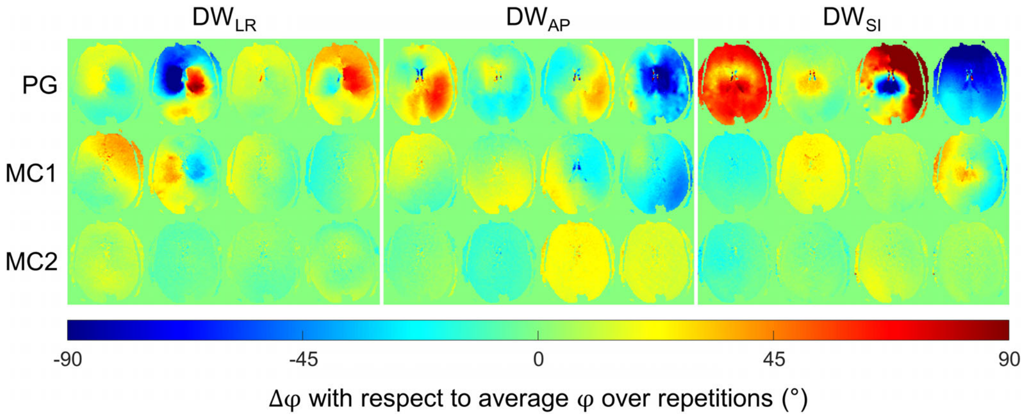

FIGURE 2 Phase maps of repeated single-shot diffusion-weighted (DW) spiral images acquired using diffusion gradients motion-compensated through the zeroth order (PG), first order (MC1), and second order (MC2). Phase maps are shown for different axes of diffusion weighting (different sections, vertically separated) and for the first 4 of 10 repetitions (different columns per section). Phase is given as the difference with respect to the phase of the complex-averaged signal over all repetitions, per diffusion direction and order of motion compensation. AP, anterior–posterior; LR, left–right; SI, superior–inferior.

In Experiment 2, evaluation of native and navigator-corrected images with respect to the corresponding MUSE image was performed in terms of normalized root mean square error (nRMSE), computed as nRMSE = $\|m_{\mathrm{ref}} - \hat{m}\|_F / \|m_{\mathrm{ref}}\|_F$, where m_{ref} is the reference (MUSE) image, $\hat{m}$ is the relevant reconstructed image (native or navigator-corrected), and $\| * \|_F$ denotes the Frobenius norm. Images in Experiments 2 and 3 were also assessed using maps of standard deviation (SD) of image magnitude across repetitions. Bias-field correction was omitted from both calculations to avoid artificial modulation.

3 | RESULTS

3.1 | Experiment 1

Phase images of repeated single-shot diffusion-weighted (DW) acquisitions using different orders of motion compensation are shown in Figure 2. Phase variability across repetitions is the most severe using PG, for which individual phase images consist of complex spatial patterns that are consistent with both rigid body (i.e., bulk) motion, which gives rise to global phase offsets and spatial phase gradients,[7] and nonrigid body motion, which contributes spatially nonlinear phase.[59] The main source of nonrigid motion is brain pulsation, which leads to the nonlinear fluctuating phase patterns originating from the ventricles. In addition, the PG phase fluctuations are considerably more volatile for the images acquired using diffusion encoding along the superior–inferior (SI) axis. On the other hand, MC1 phase images have lower repetition-wise variability, exhibiting smoother spatial variations and lower extremes, and the MC2 phase fluctuations are even further suppressed and comprise global phase offsets of low magnitude with minor spatial variations of low spatial order. Evidently, the residual uncompensated motion beyond the second order is dominated by rigid components, as nonlinear phase patterns are largely eliminated, and is effectively decoupled from the cardiac cycle.

Figure 3 illustrates the repetition-wise SD of DW phase images acquired using diffusion gradients motion-compensated through different orders for different transverse slices. As in Figure 2, phase variability weakens and manifests in flatter spatial profiles with increasing motion compensation. Phase changes are again seen to be more severe for SI diffusion encoding than for encoding along the anterior–posterior (AP) and left–right (LR) axes for PG and MC1, whereas for MC2 the phase changes are generally slightly higher for AP diffusion encoding. Over the depicted slices, the directionally averaged SD reduced by 55% and 77% with respect to PG for MC1 and MC2, respectively, of which the greatest reductions were for SI diffusion encoding at 68% and 88% for MC1 and MC2, respectively.

3.2 | Experiment 2

In Figure 4, the phase variability seen in Experiment 1 is realized in three-shot spiral and EPI acquisitions reconstructed without phase correction; images are shown for each order of motion compensation with diffusion encoding applied along the SI axis, the most critical direction in terms of phase variability. Maps of the mean and SD of image magnitude over repetitions are also shown. For both spiral and EPI, PG diffusion encoding leads to poor image quality owing to a high level of shot-to-shot

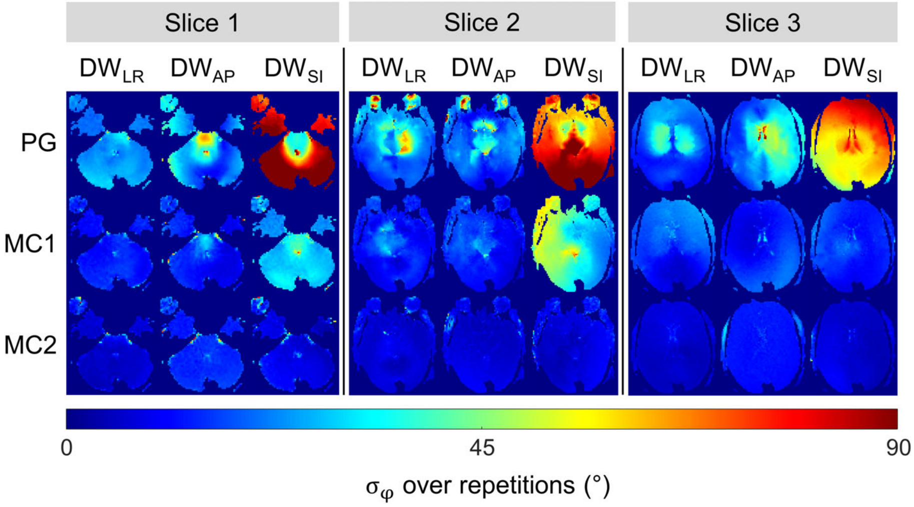

FIGURE 3 Repetition-wise SD of phase σ_φ across repeated single-shot diffusion-weighted (DW) spiral acquisitions using diffusion gradients motion-compensated through the zeroth order (PG), first order (MC1), and second order (MC2). Maps of σ_φ are shown for different axes of diffusion encoding and for multiple slices of the same volunteer. Slice 3 of this figure is the same as the slice depicted in Figure 2. AP, anterior–posterior; LR, left–right; SI, superior–inferior.

phase differences that cannot be neglected in image reconstruction. Using MC1 diffusion gradients, image quality is greatly improved, and the typical level of artifacts is reduced. Although such acquisitions often result in images devoid of perceptible artifacts, particularly for spiral trajectories, the level of phase inconsistencies in the presence of only first-order motion compensation can lead to regions of slight signal dropout for spiral and more conspicuous ghosting for EPI trajectories; these artifacts are made noticeable in the SD maps, which accentuate inconsistencies over repetitions. Using second-order motion compensation, however, typical artifacts caused by phase fluctuations are practically eliminated for spirals, yielding repeatable high image quality and a great level of consistency between each repetition and the average over repetitions, whereas ghosting occasionally occurs but remains faint for EPI.

Figure 5 compares the performance of the three forms of image reconstruction for PG, MC1, and MC2 diffusion encoding with spiral readout. For each repetition, diffusion-encoding axis, and order of motion compensation, both the native and navigator-corrected reconstructions are evaluated in terms of nRMSE with respect to the respective MUSE reconstruction, which is considered a ground truth. Furthermore, the three reconstruction methods are compared in terms of the SD of image magnitude across repetitions for each case. The benefit of the FID navigator correction is the least complete and consistent for PG, for which the elevated irreproducibility captured by the SD maps signifies considerable residual image inaccuracies. For a few cases, nRMSE is even markedly higher for the navigator-corrected than for the native reconstruction. For MC1 diffusion gradients, the performance improvement offered by the navigator phase correction is small in most cases for which the natively reconstructed image is already close to the MUSE image (less than 4% in nRMSE),

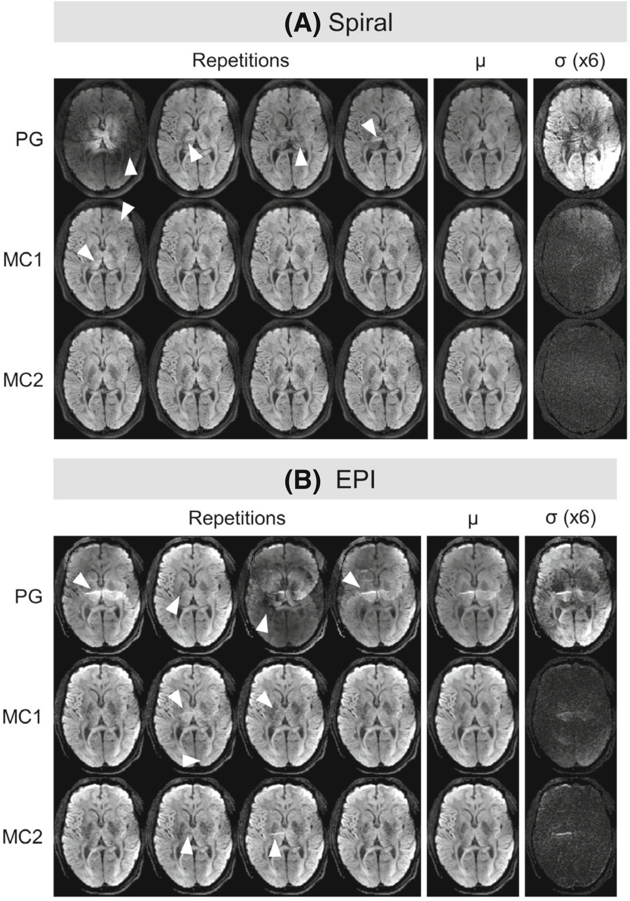

FIGURE 4 Natively reconstructed diffusion-weighted images using spiral (A) and EPI (B) trajectories for diffusion gradients motion-compensated through the zeroth order (PG), first order (MC1), and second order (MC2). For each diffusion gradient shape and readout trajectory, four repetitions of acquisitions using diffusion encoding along the superior–inferior axis are shown, as well as the mean and SD (scaled by 6) of magnitude images. Artifacts of varying strength are indicated by white arrows. The same slice of one volunteer is shown in both subfigures.

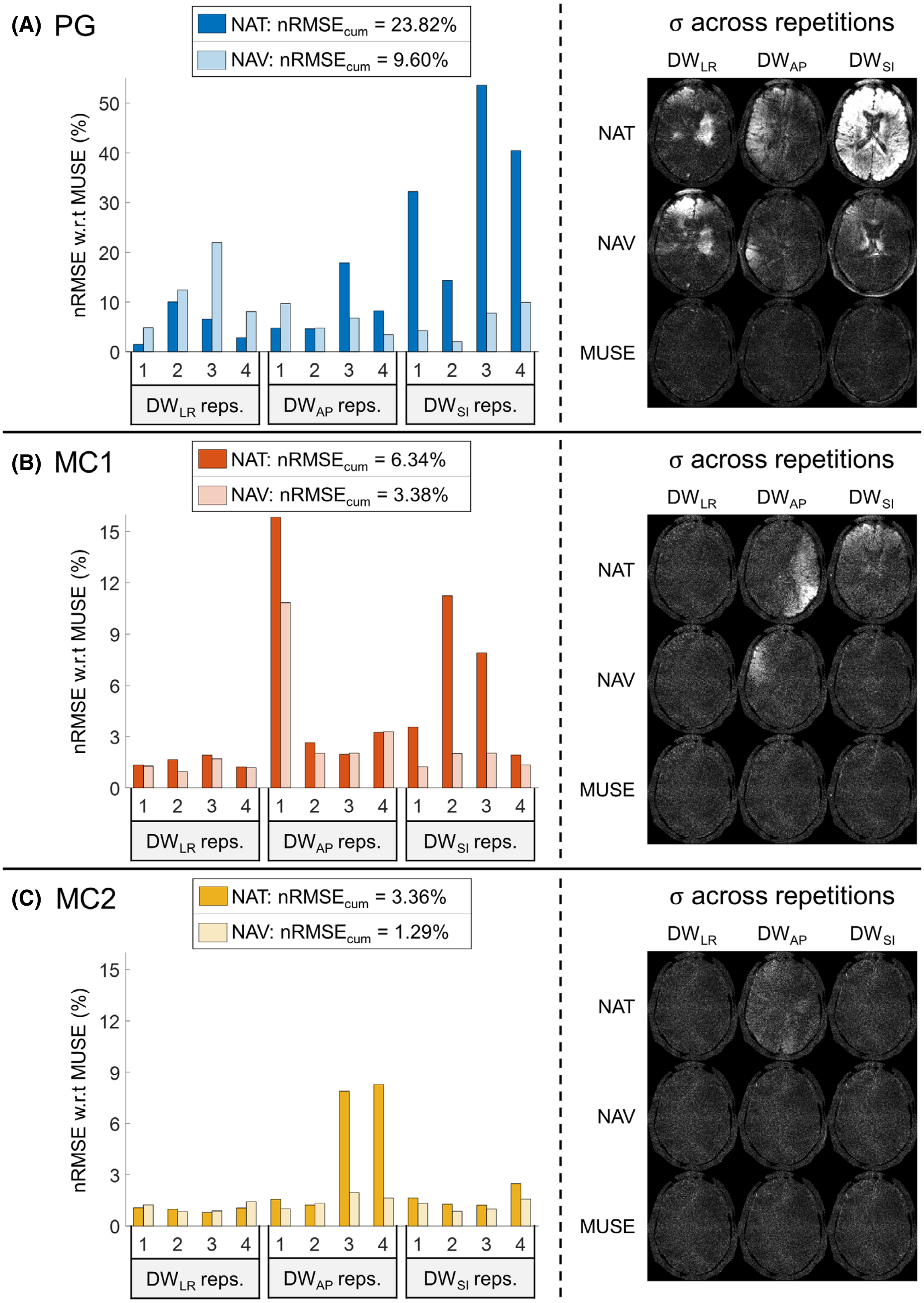

FIGURE 5 Comparison of native (NAT) and navigator phase-corrected (NAV) reconstruction for three-shot diffusion-weighted (DW) spiral acquisitions using diffusion gradients motion-compensated through the zeroth order (PG; A), first order (MC1; B), and second order (MC2; C). On the left side of each subfigure, nRMSE with respect to a MUSE reconstruction is displayed for both NAT and NAV reconstructions for all acquisitions (four repetitions of three diffusion-encoding axes); note that the vertical scaling of (B) and (C) is different than that of (A). On the right side of each subfigure, maps of the SD (of image magnitude) across repetitions per reconstruction strategy are shown for each diffusion-encoding direction. All data shown in this figure are from a representative slice of one volunteer. AP, anterior–posterior; LR, left–right; $\text{nRMSE}_{\text{cum}}$, cumulative nRMSE computed over all acquisitions per order of motion compensation; SI, superior–inferior.

representing most of the acquisitions, but more substantial when the native image has relatively larger deviations with respect to the MUSE result (with nRMSE 5%–15%). That said, the navigator correction is inadequate in a few odd cases (e.g., repetition 1 of DW_{AP}), resulting in visibly worse SD maps than for MUSE and indicating that MC1 phase variability may exceed the phase-correction capabilities of the navigator strategy. Finally, when MC2 diffusion gradients were used, navigator-corrected reconstruction again offers a small improvement in most of the cases for which native reconstruction already performs very well (less than 2% in nRMSE). A more significant benefit arises in the few cases for which native reconstruction exhibits relatively larger deviations with respect to the MUSE reconstruction (with nRMSEs 5%–10%) and is reflected in the DW_{AP} SD maps. Overall, the combination of MC2 diffusion gradients and image reconstruction using the FID navigator correction offers the best performance with respect to MUSE, consistently yielding nearly equivalent images numerically with a cumulative nRMSE of 1.29%. Importantly, for MC2 diffusion encoding the navigator correction effectively mitigates image inaccuracies in the few cases of relatively high error with native reconstruction alone.

An equivalent illustration to that shown in Figure 5 is shown for EPI readout in Figure 6. Compared with the spiral results, nRMSE values are about 1.5-2× higher for corresponding cases, and MUSE reconstructions exhibit inconsistencies that propagate as ghost profiles in the SD maps. The poorer MUSE quality for EPI can be expected because ghosting was observed in the per-shot reconstructions, which likely resulted from the higher g-factor penalty for EPI than for spiral readout;[60] this deficiency was previously shown to cause errors in 4× undersampled EPI using the same gradient system and coil.[61] The consequent apparent reduced repeatability of MUSE is conspicuous for PG and weak for MC1, but absent for MC2, demonstrating mitigation of the penalty by suppressed phase variability. Aside from these differences, the application to EPI offers the same general result as for spiral readout.

3.3 | Experiment 3

Figure 7A illustrates images from highly interleaved DW spiral acquisitions using native, navigator-corrected, and MUSE reconstructions in acquisitions using PG and MC2 diffusion encoding. Native reconstructions are riddled with artifacts for all shot counts for PG but are of high quality for MC2. Progressing to the navigator-corrected reconstructions, image quality improves for all PG images, but some false anatomical features remain; on the other hand, the MC2 navigator-corrected images are consistent with the respective native images and devoid of discernible artifacts. Finally, for both PG and MC2, the MUSE algorithm is successful for 6-shot acquisitions but fails for 8- and 10-shot acquisitions, producing corrupted images with particularly conspicuous hyperintensities around the ventricles because of faulty per-shot reconstructions.

In Figure 7B, an equivalent set of images is shown for highly interleaved EPI acquisitions. It can again be observed that both native and navigator phase-corrected images are visibly untroubled at both interleaving factors using MC2 gradients but produce strong artifacts for PG. Using MUSE, however, artifacts progressively worsen going from five to seven shots and are worse than those seen for three-shot EPI in Figure 6.

To evaluate the repeatability of navigator-corrected reconstruction using MC2 diffusion sensitization in highly interleaved acquisitions, Figure 8 depicts multiple repetitions for each interleaving factor and readout trajectory, in addition to the repetition-wise means and SDs. The SD maps indicate the presence of intensity disparities that are inconsistent with pure noise and anatomical mismatch, which would manifest in spatial homogeneity and edge enhancement in the SD maps, respectively. Moreover, these intensity disparities are more pronounced than those seen in three-shot acquisitions based on Figures 5 and 6, reflecting reduced repeatability at higher interleaving factors. That said, the images here are very consistent, and the differences are hardly discernible in individual images.

4 | DISCUSSION

Second-order motion-compensated diffusion encoding most effectively suppressed phase variability in repeated single-shot acquisitions, permitting just small residual phase fluctuations of low spatial order. Consequently, multi-shot MC2 images were largely devoid of artifacts when reconstructed without phase correction and were consistently improved and of high quality when reconstructed with a simple channel-wise phase correction based on FID navigation. These navigator-corrected images were in close agreement with MUSE reconstructions for a standard interleaving factor of three and were of higher quality than MUSE images in highly interleaved acquisitions, in which the modeling constraints of MUSE led to severe artifacts.

The superiority of MC2 over MC1 diffusion encoding in multi-shot experiments was demonstrated in Experiment 2, in which MC1 native and navigator-corrected images had more artifacts and higher nRMSEs with respect to MUSE than those of MC2. This performance disparity indicates that the critical corrupting motions are chiefly confined to the second temporal order and below.

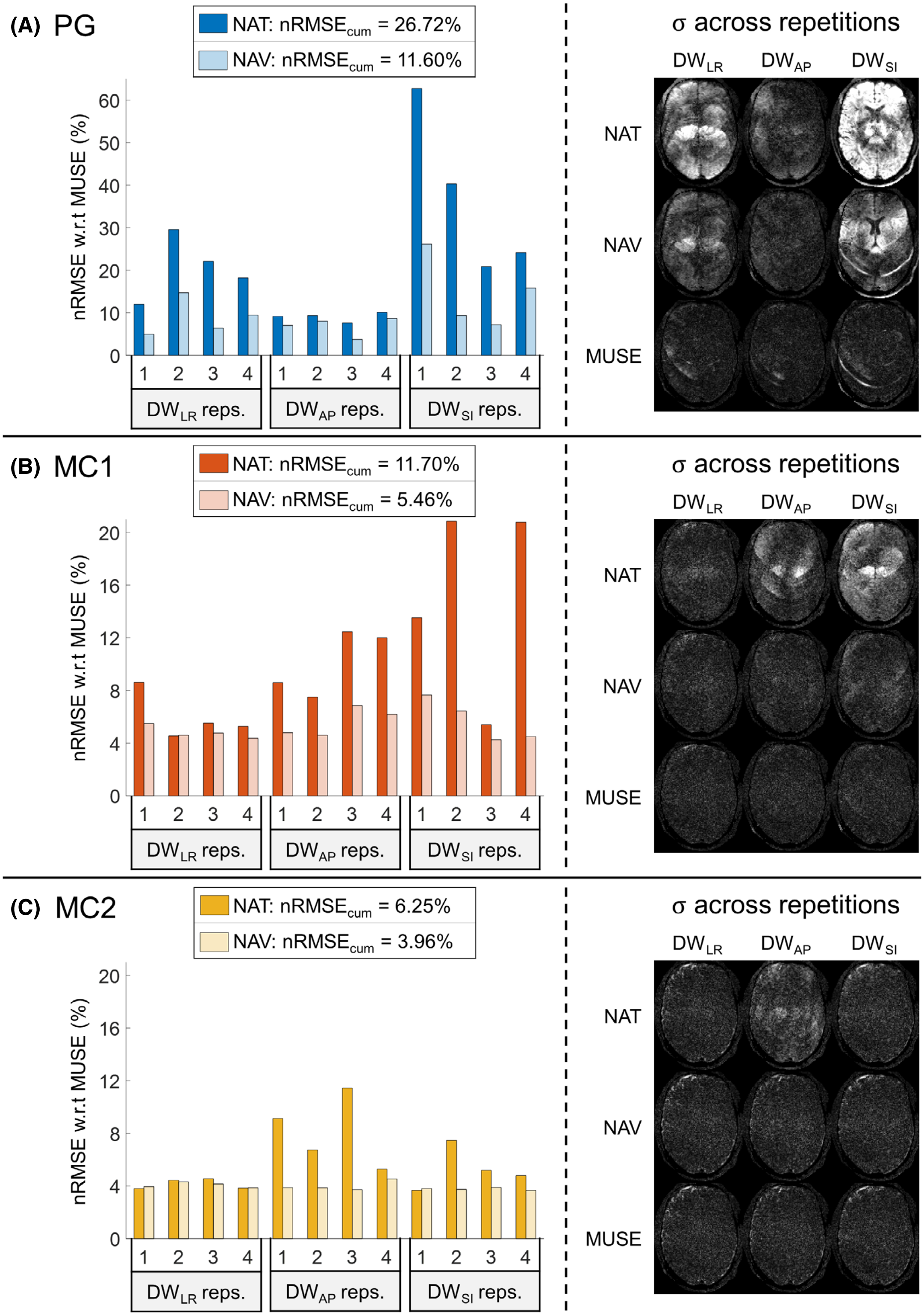

FIGURE 6 Comparison of native (NAT) and navigator phase-corrected (NAV) reconstruction for three-shot diffusion-weighted (DW) EPI acquisitions using diffusion gradients motion-compensated through the zeroth order (PG; A), first order (MC1; B), and second order (MC2; C). On the left side of each subfigure, nRMSE with respect to a MUSE reconstruction is displayed for both NAT and NAV reconstructions for all acquisitions (four repetitions of three diffusion-encoding axes); note that the vertical scaling of (B) and (C) is different than that of (A). On the right side of each subfigure, maps of the SD (of image magnitude) across repetitions per reconstruction strategy are shown for each diffusion-encoding direction. All data shown in this figure are from a representative slice of one volunteer. AP, anterior–posterior; LR, left–right; nRMSE$_{cum}$, cumulative nRMSE computed over all acquisitions per order of motion compensation; SI, superior–inferior.

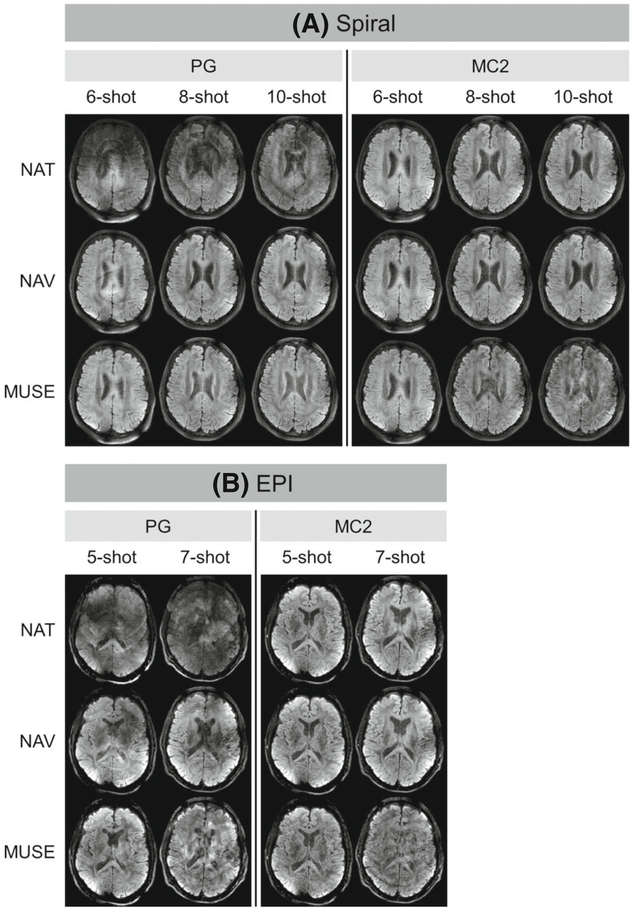

FIGURE 7 Comparison of reconstruction methods for highly interleaved diffusion acquisitions with motion compensation through the zeroth order (PG) and second order (MC2). Native (NAT), navigator phase-corrected (NAV), and MUSE images are shown for spiral (A) and EPI (B) acquisitions with different interleaving factors per readout type. For each column of the figure, all three reconstructed images correspond to the same acquisition, that is, one repetition of superior–inferior axis diffusion encoding. (A) and (B) depict different slices of the same volunteer.

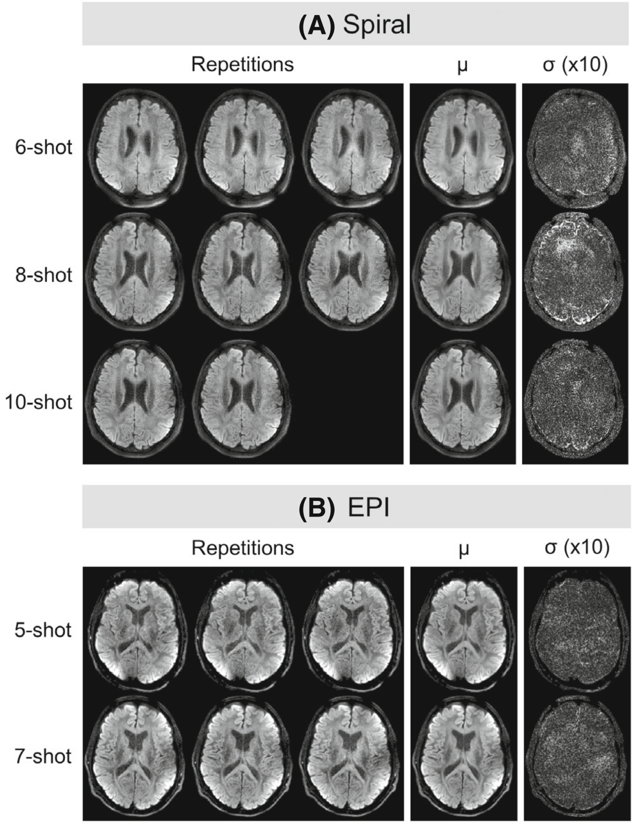

FIGURE 8 Navigator-corrected diffusion-weighted images for repeated highly interleaved spiral (A) and EPI (B) acquisitions using diffusion gradients motion-compensated through the second order. Images acquired using superior–inferior axis diffusion encoding are shown for all acquired repetitions at each interleaving factor per readout trajectory, in addition to the repetition-wise mean and SD (scaled by 10) of magnitude images per selection. The same slices as displayed in (A) and (B) of Figure 7 are shown in the respective subfigures here.

This notion is supported by the abatement of nonrigid motions—namely, brain pulsation—upon second-order motion compensation, given that brain pulsation was found to be the dominant source of artifacts in multi-shot brain DWI.[62] As such, the remaining motions at higher orders likely constitute fast bulk head movements, such as cardiac-induced rigid head motion and involuntary movement, and result in phase variations of low spatial complexity that are more satisfactorily correctable than the spatially nonlinear phase resulting from nonrigid motions. That said, higher-order motions may still violate the constraints of the navigator approach, albeit marginally and infrequently, as seen in Figure 8. Because motion is unrelated to sequence timing, such violations are likely probabilistic in nature, such that additional shots entail additional potentially deficient navigator measurements, and exacerbated by dynamic interactions between subject position and MR fields;[63] these interactions would bias the navigator-based phase measurements and likely worsen with increasing scan time because a broader range of displacements can be expected. Nonetheless, in light of the high consistency of satisfactory correction with second-order motion compensation, the diminishing returns of even higher orders of motion compensation will have to be weighed against the additional encoding demands.

The key advantage of motion-compensated diffusion sensitization is that phase correction requires reduced spatial fidelity or, analogously, spatial phase constraints imparted by a given correction algorithm are better satisfied. The proximity of the MC2 navigator-corrected images to MUSE reconstructions at interleaf factors for which MUSE succeeded illustrates that correction of low effective spatial specificity was sufficient and that phase correction of higher spatial resolution was dispensable. On the other hand, the FID navigator approach was deficient with uncompensated diffusion sensitization, for which MUSE was required to produce uncorrupted images.

Comparison of native and navigator-corrected images was done with respect to MUSE, which represents a present standard for image reconstruction in multi-shot DWI. Several other multi-shot diffusion reconstruction strategies outperform MUSE, particularly at higher interleaving factors, but often entail considerably more computation time than MUSE. Owing to the reduced vulnerability of phase variability to nonrigid motions, our strategy could reconstruct up to 10-shot spiral images acquired with an eight-channel coil, matching that achieved using POCS-ICE.[19] Going forward, motion-compensated diffusion gradients could be used in conjunction with such advanced reconstruction algorithms for retrospective phase correction to extend the present limits of image accuracy and convergence time for a given interleaf factor owing to the higher fidelity of per-shot phase maps to the constraints. Moreover, further improvement could be attained by correcting for macroscopic motion between interleaves, which was not done in the reconstructions performed here.

The key drawback of using motion-compensated diffusion gradients is the SNR penalty incurred by the resultant increase in TE, which rises with the order of motion compensation; however, this penalty becomes weaker as gradient strength increases. Figure 9 illustrates the TE-based SNR reduction incurred by using MC1 and MC2 gradients rather than PG for different b-values and gradient strengths and for spiral and EPI readout; TE can be minimized in accordance with EPI readout duration[64] and is independent of spiral readout duration. Assuming a representative white-matter T_2 of 80 ms,[65] SNR reductions in the spiral acquisitions performed here were approximately 15% and 19% when using MC1 and MC2 diffusion gradients, respectively, instead of PG; for an EPI readout lasting 30 ms (representing the three-shot acquisitions here), the corresponding SNR reductions were 20% and 23%. The slightly higher penalties of MC2 were decidedly worthwhile for the resultant improved image accuracy. For a more standard modern clinical gradient strength of 80 mT/m, SNR penalties for the b-value used here using a spiral trajectory would be 24% and 33% for MC1 and MC2, respectively, and 30% and 36% using EPI. On the other hand, at the time of the previous motion-compensated multi-shot diffusion experiments,[41–44] the SNR penalties would have been 52% and 63% for MC1 and MC2, respectively, at a contemporary gradient amplitude of 20 mT/m and using EPI. Evidently, the former disadvantage of motion-compensated diffusion encoding has considerably reduced, and the adoption of less-efficient diffusion encoding for suppression of phase variability will become even more appealing as gradient hardware progresses.

Another consequence of using motion-compensated diffusion gradients is that the frequency encoding of diffusivity is different with respect to PG, resulting in slightly different image contrast due to frequency-dependent restricted diffusion.[66] That said, diffusivities are only weakly dependent on frequency in human brain tissue—mean diffusivity can be expected to increase by up to about 5% for MC2 or MC1 with respect to PG measurements based on the encoded centroid frequencies here and reported diffusion dispersion rates[67]—and such changes would not meaningfully affect the experiment.

Both EPI and spiral results are presented in this work, with differing results. For MC2 diffusion gradients, spiral trajectories proved to be superior at each level of phase correction in image reconstruction, agreeing with the reported general favorability of spirals in single-shot diffusion experiments,[60,68] even though shot-to-shot phase variability resulting from diffusion encoding is independent of readout trajectory. Stronger artifacts likely result for EPI because uncorrected phase inconsistencies among segments consisting of regularly interleaved Cartesian k-space lines result in concentrated aliasing, whereas the spiral sampling pattern effectively disperses the effects of uncorrected shot-wise phase variations. This consideration holds true for all forms of retrospective phase correction because some degree of misestimation of per-shot phase is inherent to all such methods, namely, due to the common assumption of spatially smooth phase maps. It is also worth noting that for the navigator phase-correction method, the navigation interval is time-adjacent to the acquisition of the spin echo for spiral but not for EPI; therefore, the spiral navigator signal suffers considerably less T_2* decay and has better SNR. Furthermore, during the navigator to spin-echo time separation for EPI, the readout gradients introduce small additional moments that can alter the spatial phase distribution at the spin echo with respect to that present during navigation, thereby reducing the accuracy of the navigator correction.

The evaluation of motion-compensated diffusion encoding in multi-shot acquisitions as presented here represents the case at a standard b-value of 1000 s/mm^2, but the efficacy of the technique can be expected to vary with b-value. It can be shown that the nth-order moment, m_n, of a diffusion gradient waveform under uniform contraction or expansion and constant amplitude scales with b as $m_n \propto b^{(n+1)/3}$. As such, motion-compensated diffusion gradients will less effectively suppress shot-to-shot phase variability as b increases. Future work should assess such effect on the overall performance of interleaved, motion-compensated diffusion acquisitions with respect to b-value.

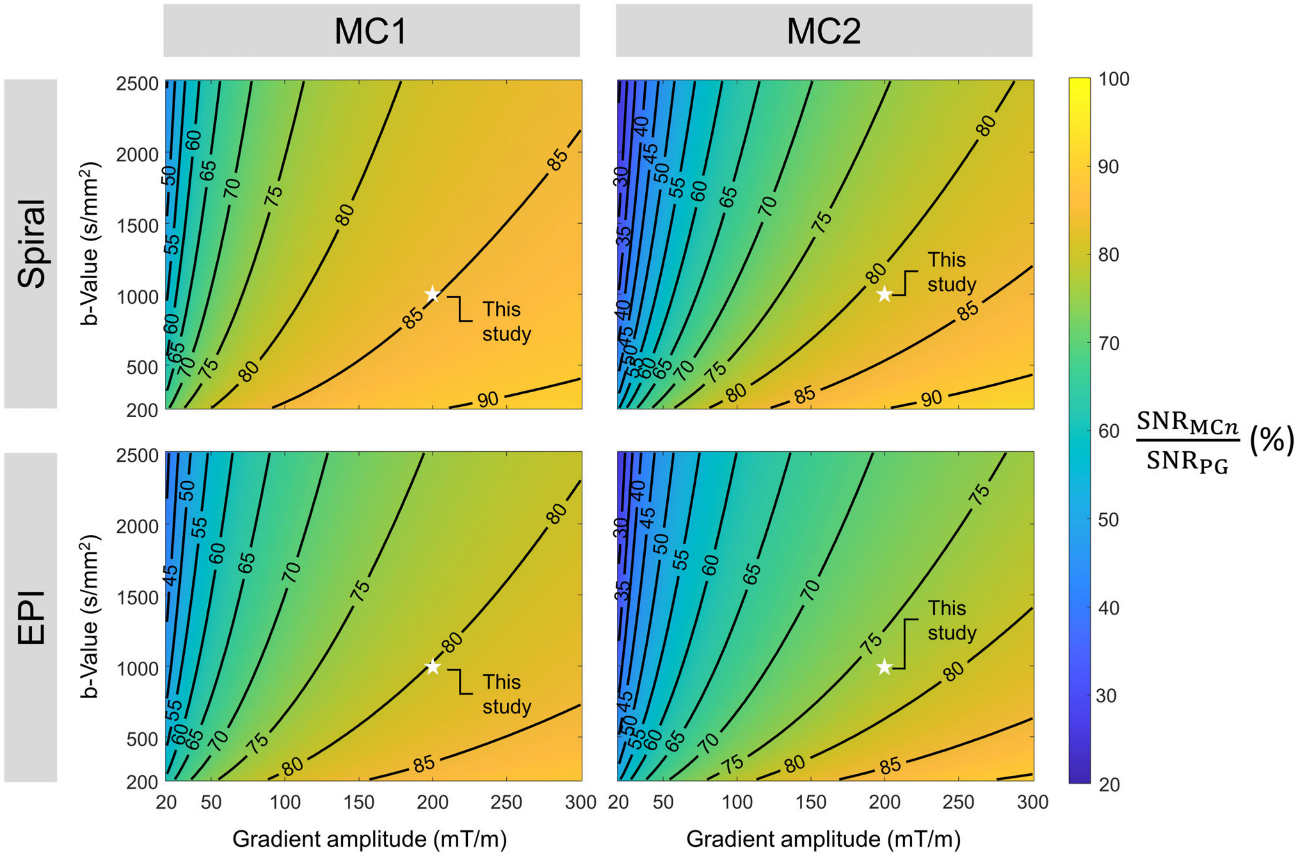

FIGURE 9 Relative SNR using diffusion gradients motion-compensated through the first order (MC1) and second order (MC2) with respect to using conventional zeroth-order–compensated pulsed diffusion gradients (PG) for spiral and EPI acquisition. Relative SNR was obtained using the difference between the minimum TEs attainable using diffusion gradients with different orders of motion compensation given a b-value and gradient amplitude, assuming a representative T_2 of white matter (80 ms). In computing the minimum TEs, gradient waveforms were assumed to have a gradient rise time, τ, of 0.33 ms (matching what can be achieved on the gradient system used here) and a gap between pulses (i.e., for the 180° RF pulse) of 4.5 ms for MC1 and PG; the gap is predefined as $(\delta_1 + \delta_2)/3 - 3\tau$ for MC2, where δ_1 and δ_2 are the durations of the positive and negative lobes of the first bipolar pulse, respectively (see Figure S1). Moreover, TEs for EPI were computed assuming an acquisition window of 30 ms. It is worth noting that the SNR penalties due to motion compensation reduce for EPI as the acquisition window shortens—equivalently in practice, as the interleaving factor increases—and increase as the acquisition window lengthens.

Although DTI was not performed in this work, the advantages of moment nulling demonstrated here can be expected to equally apply in multi-shot DTI acquisitions. An additional consideration that must be made in this prospective application is the behavior of eddy currents, which cause artifacts (in particular, distortions in EPI acquisitions) that depend on the direction and form of diffusion encoding and must be corrected for the sake of image registration. Such artifacts were mitigated in this work by the incorporation of dynamic field information in image reconstruction, thereby precluding any potential dependence of eddy-current–related artifacts on the choice of PG, MC1, or MC2. That said, retrospective analysis of the field evolution resulting from diffusion encoding demonstrated that eddy currents only had considerably different strengths in the zeroth order (of spherical harmonics), for which eddy currents were weakest for MC1 and strongest for PG (Figure S2). This finding agrees with several studies[69–71] that have reported weaker eddy currents using bipolar diffusion gradients (of the same form as MC1 used here) instead of monopolar gradients, indicating that both MC1 and MC2 diffusion gradients are favorable in terms of eddy currents with respect to conventional PG.

This work represents a novel deployment of motion-compensated diffusion encoding as a means of reducing the requirements of retrospective phase correction in multi-shot brain acquisitions, but moment-nulled diffusion gradients have also been used in multi-shot acquisitions outside the brain. In cardiac imaging, diffusion-prepared sequences with multi-shot acquisition have incorporated motion-compensated diffusion encoding.[34,35] The key distinction of such sequences is that diffusion encoding is not repeated with each acquisition block and is instead performed only once per acquisition volume, so shot-to-shot phase variability does not need to be addressed; that said, any nonzero phase accumulation due to motion introduces erroneous additional signal weighting that biases diffusion coefficients in diffusion-prepared sequences. In pulse sequences equivalent to those used here, motion-robust diffusion encoding[72] consisting of optimized gradient waveforms with reduced but not nulled first-order moments was recently shown to be advantageous in single-shot and multi-shot EPI of the kidney;[73] in contrast to our work, the use of the modified diffusion gradients was complemented by MUSE in the multi-shot acquisitions rather than investigated as an alternative. That said, it is likely that more highly spatially resolved phase correction cannot be averted in such organs that suffer substantially more motion than the brain, even when shot-to-shot phase variability is reduced by motion compensation.

5 | CONCLUSION

Second-order motion-compensated diffusion sensitization in human brain imaging effectively suppressed shot-to-shot phase fluctuations and sensitivity to nonrigid body motions—in particular, brain pulsation—yielding small phase differences dominated by components of low spatial order. The benign effect of the residual uncompensated motions, which were primarily rigid, permitted consistent high image quality using a simple shot-to-shot phase correction of low spatial specificity based on an FID navigator. These images were in close agreement with MUSE reconstructions for a standard interleaving factor and outperformed MUSE for high interleaving factors, circumventing intrinsic limitations associated with modeling phase variability. Motion-compensated diffusion encoding faces a substantially lower inherent SNR penalty than in previous generations due to advancements in gradient hardware, thereby offering a viable change in paradigm with respect to retrospective phase-correction techniques for the acquisition of highly resolved diffusion data.

CONFLICT OF INTEREST

Klaas Paul Pruessmann holds a research agreement with and receives research support from Philips and is a shareholder of GyroTools LLC.

ACKNOWLEDGEMENT

Open access funding provided by Eidgenossische Technische Hochschule Zurich.

ORCID

Eric Seth Michael https://orcid.org/0000-0002-2513-4254
Franciszek Hennel https://orcid.org/0000-0003-0043-9921
Klaas Paul Pruessmann https://orcid.org/0000-0003-0009-8362

REFERENCES

1. Wilm BJ, Hennel F, Roesler MB, Weiger M, Pruessmann KP. Minimizing the echo time in diffusion imaging using spiral readouts and a head gradient system. *Magn Reson Med.* 2020;84:3117-3127.
2. Stejskal EO, Tanner JE. Spin diffusion measurements: spin echoes in the presence of a time-dependent field gradient. *J Chem Phys.* 1965;42:288-292.
3. Norris DG. Implications of bulk motion for diffusion-weighted imaging experiments: effects, mechanisms, and solutions. *J Magn Reson Imaging.* 2001;13:486-495.
4. Holdsworth SJ, O'Halloran R, Setsompop K. The quest for high spatial resolution diffusion-weighted imaging of the human brain in vivo. *NMR Biomed.* 2019;32:e4056.
5. Ehman RL, Felmlee JP. Adaptive technique for high-definition MR imaging of moving structures. *Radiology.* 1989;173:255-263.
6. Ordidge RJ, Helpern JA, Qing ZX, Knight RA, Nagesh V. Correction of motional artifacts in diffusion-weighted MR images using navigator echoes. *Magn Reson Imaging.* 1994;12:455-460.
7. Anderson AW, Gore JC. Analysis and correction of motion artifacts in diffusion weighted imaging. *Magn Reson Med.* 1994;32:379-387.
8. de Crespigny AJ, Marks MP, Enzmann DR, Moseley ME. Navigated diffusion imaging of normal and ischemic human brain. *Magn Reson Med.* 1995;33:720-728.
9. Butts K, de Crespigny A, Pauly JM, Moseley M. Diffusion-weighted interleaved echo-planar imaging with a pair of orthogonal navigator echoes. *Magn Reson Med.* 1996;35:763-770.
10. Butts K, Pauly J, de Crespigny A, Moseley M. Isotropic diffusion-weighted and spiral-navigated interleaved EPI for routine imaging of acute stroke. *Magn Reson Med.* 1997;38:741-749.
11. Liu C, Bammer R, Kim D-H, Moseley ME. Self-navigated interleaved spiral (SNAILS): application to high-resolution diffusion tensor imaging. *Magn Reson Med.* 2004;52:1388-1396.
12. Liu C, Moseley ME, Bammer R. Simultaneous phase correction and SENSE reconstruction for navigated multi-shot DWI with non-cartesian k-space sampling. *Magn Reson Med.* 2005;54:1412-1422.
13. Pruessmann KP, Weiger M, Scheidegger MB, Boesiger P. SENSE: sensitivity encoding for fast MRI. *Magn Reson Med.* 1999;42:952-962.
14. Pruessmann KP, Weiger M, Börnert P, Boesiger P. Advances in sensitivity encoding with arbitrary k-space trajectories. *Magn Reson Med.* 2001;46:638-651.
15. Chen N-K, Guidon A, Chang H-C, Song AW. A robust multi-shot scan strategy for high-resolution diffusion weighted MRI enabled by multiplexed sensitivity-encoding (MUSE). *Neuroimage.* 2013;72:41-47.

16. Truong T-K, Guidon A. High-resolution multishot spiral diffusion tensor imaging with inherent correction of motion-induced phase errors. *Magn Reson Med*. 2014;71:790-796.
17. Zhang Z, Huang F, Ma X, Xie S, Guo H. Self-feeding MUSE: a robust method for high resolution diffusion imaging using interleaved EPI. *Neuroimage.* 2015;105:552-560.
18. Chu M-L, Chang H-C, Chung H-W, Truong T-K, Bashir MR, Chen NK. POCS-based reconstruction of multiplexed sensitivity encoded MRI (POCSMUSE): a general algorithm for reducing motion-related artifacts. *Magn Reson Med.* 2015;74:1336-1348.
19. Guo H, Ma X, Zhang Z, Zhang B, Yuan C, Huang F. POCS-enhanced inherent correction of motion-induced phase errors (POCS-ICE) for high-resolution multishot diffusion MRI. *Magn Reson Med.* 2016;75:169-180.
20. Hu Z, Ma X, Truong T-K, Song AW, Guo H. Phase-updated regularized SENSE for navigator-free multishot diffusion imaging. *Magn Reson Med.* 2017;78:172-181.
21. Mani M, Jacob M, Kelley D, Magnotta V. Multi-shot sensitivity-encoded diffusion data recovery using structured low-rank matrix completion (MUSSELS). *Magn Reson Med.* 2017;78:494-507.
22. Hu Y, Levine EG, Tian Q, et al. Motion-robust reconstruction of multishot diffusion-weighted images without phase estimation through locally low-rank regularization. *Magn Reson Med.* 2019;81:1181-1190.
23. Mani M, Aggarwal HK, Magnotta V, Jacob M. Improved MUSSELS reconstruction for high-resolution multi-shot diffusion weighted imaging. *Magn Reson Med.* 2020;83:2253-2263.
24. Mani M, Jacob M, McKinnon G, et al. SMS MUSSELS: a navigator-free reconstruction for simultaneous multi-slice-accelerated multi-shot diffusion weighted imaging. *Magn Reson Med.* 2020;83:154-169.
25. Guhaniyogi S, Chu M-L, Chang H-C, Song AW, Chen N-K. Motion immune diffusion imaging using augmented MUSE for high-resolution multi-shot EPI. *Magn Reson Med.* 2016;75:639-652.
26. Dong Z, Wang F, Ma X, Dai E, Zhang Z, Guo H. Motion-corrected k-space reconstruction for interleaved EPI diffusion imaging. *Magn Reson Med.* 2018;79:1992-2002.
27. Steinhoff M, Nehrke K, Mertins A, Börnert P. Segmented diffusion imaging with iterative motion-corrected reconstruction (SEDIMENT) for brain echo-planar imaging. *NMR Biomed.* 2020;33:e4185.
28. Riedel M, Setsompop K, Mertins A, Börnert P. Segmented simultaneous multi-slice diffusion-weighted imaging with navigated 3D rigid motion correction. *Magn Reson Med.* 2021;86:1701-1717.
29. Chang H-C, Guhaniyogi S, Chen N-K. Interleaved diffusion-weighted EPI improved by adaptive partial-Fourier and multiband multiplexed sensitivity-encoding reconstruction. *Magn Reson Med.* 2015;73:1872-1884.
30. Dai E, Ma X, Zhang Z, Yuan C, Guo H. Simultaneous multislice accelerated interleaved EPI DWI using generalized blipped-CAIPI acquisition and 3D k-space reconstruction. *Magn Reson Med.* 2017;77:1593-1605.
31. Dai E, Mani M, McNab JA. Multi-band multi-shot diffusion MRI reconstruction with joint usage of structured low-rank constraints and explicit phase mapping. *Magn Reson Med.* 2023;89:95-111.
32. Hu Y, Xu Y, Tian Q, et al. RUN-UP: accelerated multishot diffusion-weighted MRI reconstruction using an unrolled network with U-net as priors. *Magn Reson Med.* 2021;85:709-720.
33. Chen H, Dai K, Zhong S, et al. High-resolution multi-shot diffusion-weighted MRI combining markerless prospective motion correction and locally low-rank constrained reconstruction. *Magn Reson Med.* 2023;89:605-619.
34. Nguyen C, Fan Z, Sharif B, et al. In vivo three-dimensional high resolution cardiac diffusion-weighted MRI: a motion compensated diffusion-prepared balanced steady-state free precession approach. *Magn Reson Med.* 2014;72:1257-1267.
35. Xie Y, Yu W, Fan Z, et al. High resolution 3D diffusion cardiovascular magnetic resonance of carotid vessel wall to detect lipid core without contrast media. *J Cardiovasc Magn Reson.* 2014;16:67.
36. Stoeck CT, von Deuster C, Genet M, Atkinson D, Kozerke S. Second-order motion-compensated spin echo diffusion tensor imaging of the human heart. *Magn Reson Med.* 2016;75:1669-1676.
37. Ozaki M, Inoue Y, Miyati T, et al. Motion artifact reduction of diffusion-weighted MRI of the liver: use of velocity-compensated diffusion gradients combined with tetrahedral gradients. *J Magn Reson Imaging.* 2013;37:172-178.
38. Geng R, Zhang Y, Starekova J, et al. Characterization and correction of cardiovascular motion artifacts in diffusion-weighted imaging of the pancreas. *Magn Reson Med.* 2021;86:1956-1969.
39. McTavish S, Van AT, Peeters JM, et al. Motion compensated renal diffusion weighted imaging. *Magn Reson Med.* 2023;89:144-160.
40. Kara D, Koenig K, Lowe M, Nguyen CT, Sakaie K. Facilitating diffusion tensor imaging of the brain during continuous gross head motion with first and second order motion compensating diffusion gradients. *Magn Reson Med.* 2024;91:1556-1566.
41. Prasad PV, Nalcioglu O. A modified pulse sequence for in vivo diffusion imaging with reduced motion artifacts. *Magn Reson Med.* 1991;18:116-131.
42. Christiansen P, Gideon P, Thomsen C, Stubgaard M, Henriksen O, Larsson HBW. Increased water self-diffusion in chronic plaques and in apparently normal white matter in patients with multiple sclerosis. *Acta Neurol Scand.* 1993;87:195-199.
43. Brockstedt S, Thomsen C, Wirestam R, et al. Use of an enhanced gradient system for diffusion MR imaging with motion-artifact reduction. *Acta Radiol.* 1995;36:662-670.
44. Clark CA, Barker GJ, Tofts PS. Improved reduction of motion artifacts in diffusion imaging using navigator echoes and velocity compensation. *J Magn Reson.* 2000;142:358-363.
45. Setsompop K, Kimmlingen R, Eberlein E, et al. Pushing the limits of in vivo diffusion MRI for the human connectome project. *Neuroimage.* 2013;80:220-233.
46. Weiger M, Overweg J, Rösler MB, et al. A high-performance gradient insert for rapid and short-T2 imaging at full duty cycle. *Magn Reson Med.* 2018;79:3256-3266.
47. Foo TKF, Tan ET, Vermilyea ME, et al. Highly efficient head-only magnetic field insert gradient coil for achieving simultaneous high gradient amplitude and slew rate at 3.0T (MAGNUS) for brain microstructure imaging. *Magn Reson Med.* 2020;83:2356-2369.
48. Huang SY, Witzel T, Keil B, et al. Connectome 2.0: developing the next-generation ultra-high gradient strength human

MRI scanner for bridging studies of the micro-, meso- and macro-connectome. *Neuroimage.* 2021;243:118530.

49. Davids M, Dietz P, Ruyters G, et al. Peripheral nerve stimulation informed design of a high-performance asymmetric head gradient coil. *Magn Reson Med.* 2023;90:784-801.
50. Rösler MB, Leussler C, Brunner DO, et al. A transmit-receive array for brain imaging with a high-performance gradient insert. *Magn Reson Med.* 2020;84:2278-2289.
51. Gamper U, Boesiger P, Kozerke S. Diffusion imaging of the in vivo heart using spin echoes—considerations on bulk motion sensitivity. *Magn Reson Med.* 2007;57:331-337.
52. Welsh CL, DiBella EVR, Hsu EW. Higher-order motion-compensation for in vivo cardiac diffusion tensor imaging in rats. *IEEE Trans Med Imaging.* 2015;34:1843-1853.
53. Hennel F. Image-based reduction of artifacts in multishot echo-planar imaging. *J Magn Reson.* 1998;134:206-213.
54. Dietrich BE, Brunner DO, Wilm BJ, et al. A field camera for MR sequence monitoring and system analysis. *Magn Reson Med.* 2016;75:1831-1840.
55. Wilm BJ, Barmet C, Pavan M, Pruessmann KP. Higher order reconstruction for MRI in the presence of spatiotemporal field perturbations. *Magn Reson Med.* 2011;65:1690-1701.
56. Hu X, Kim S-G. Reduction of signal fluctuation in functional MRI using navigator echoes. *Magn Reson Med.* 1994;31:495-503.
57. Kellner E, Dhital B, Kiselev VG, Reisert M. Gibbs-ringing artifact removal based on local subvoxel-shifts. *Magn Reson Med.* 2016;76:1574-1581.
58. Ashburner J, Friston KJ. Unified segmentation. *Neuroimage.* 2005;26:839-851.
59. Miller KL, Pauly JM. Nonlinear phase correction for navigated diffusion imaging. *Magn Reson Med.* 2003;50:343-353.
60. Lee Y, Wilm BJ, Brunner DO, et al. On the signal-to-noise ratio benefit of spiral acquisition in diffusion MRI. *Magn Reson Med.* 2021;85:1924-1937.
61. Hennel F, Wilm BJ, Roesler MB, Weiger M, Dietrich B, Pruessmann KP. Echo-planar imaging of the human head with 100 mT/m gradients and high-order modeling of eddy current fields. *Magn Reson Med.* 2020;84:751-761.
62. Jiang H, Golay X, van Zijl PCM, Mori S. Origin and minimization of residual motion-related artifacts in navigator-corrected segmented diffusion-weighted EPI of the human brain. *Magn Reson Med.* 2002;47:818-822.
63. Maclaren J, Herbst M, Speck O, Zaitsev M. Prospective motion correction in brain imaging: a review. *Magn Reson Med.* 2013;69:621-636.
64. Peña-Nogales Ó, Zhang Y, Wang X, et al. Optimized diffusion-weighting gradient waveform design (ODGD) formulation for motion compensation and concomitant gradient nulling. *Magn Reson Med.* 2019;81:989-1003.
65. Wansapura JP, Holland SK, Dunn RS, Ball WS Jr. NMR relaxation times in the human brain at 3.0 Tesla. *J Magn Reson Imaging.* 1999;9:531-538.
66. Does MD, Parsons EC, Gore JC. Oscillating gradient measurements of water diffusion in normal and globally ischemic rat brain. *Magn Reson Med.* 2003;49:206-215.
67. Arbabi A, Kai J, Khan AR, Baron CA. Diffusion dispersion imaging: mapping oscillating gradient spin-echo frequency dependence in the human brain. *Magn Reson Med.* 2020;83:2197-2208.
68. Feizollah S, Tardif CL. High-resolution diffusion-weighted imaging at 7 Tesla: single-shot readout trajectories and their impact on signal-to-noise ratio, spatial resolution and accuracy. *Neuroimage.* 2023;274:120159.
69. Trudeau JD, Dixon WT, Hawkins J. The effect of inhomogeneous sample susceptibility on measured diffusion anisotropy using NMR imaging. *J Magn Reson Ser B.* 1995;108:22-30.
70. Alexander AL, Tsuruda JS, Parker DL. Elimination of eddy current artifacts in diffusion-weighted echo-planar images: the use of bipolar gradients. *Magn Reson Med.* 1997;38:1016-1021.
71. Chan RW, von Deuster C, Giese D, et al. Characterization and correction of eddy-current artifacts in unipolar and bipolar diffusion sequences using magnetic field monitoring. *J Magn Reson.* 2014;244:74-84.
72. Zhang Y, Peña-Nogales Ó, Holmes JH, Hernando D. Motion-robust and blood-suppressed M1-optimized diffusion MR imaging of the liver. *Magn Reson Med.* 2019;82:302-311.
73. Geng R, Zhang Y, Rice J, et al. Motion-robust, blood-suppressed, reduced-distortion diffusion MRI of the liver. *Magn Reson Med.* 2023;89:908-921.

SUPPORTING INFORMATION

Additional supporting information may be found in the online version of the article at the publisher's website.

Figure S1. Diffusion-encoding gradient waveforms achieving motion compensation through the zeroth order (PG), first order (MC1), and second order (MC2). Gradient waveforms include the effect of the refocusing RF pulse. The zeroth-order–compensated gradients shown here were used in all spiral acquisitions; those used in EPI acquisitions had larger Δ and smaller δ for all interleaving factors, with both Δ and δ adjusted based on the duration of the respective acquisition window to minimize TE.

Figure S2. Eddy currents resulting from diffusion gradients motion-compensated through the zeroth order (PG), first order (MC1), and second order (MC2) for different axes of diffusion encoding (different sections, vertically separated). All plots reflect the temporal evolutions of the maximum phase accrual (in radians) resulting from diffusion sensitization during a single shot of a three-shot spiral readout on a sphere of radius 100 mm. These evolutions are given in terms of coefficients, k_l, of spherical harmonic basis functions of different orders (different rows) and were computed using the fitted field dynamics of the first shot (22.1 ms acquisition interval) of representative three-shot spiral acquisitions. The contributions resulting from diffusion encoding were isolated by computing differences between spherical harmonic field coefficients of DW acquisitions and corresponding $b = 0\,\mathrm{s/mm}^2$ acquisitions.

Legend entries correspond to all plots within the same row. Note that vertical scaling is consistent within rows except for the first row (zeroth-order eddy currents), for which the vertical scale is significantly larger for diffusion encoding along the SI axis than for diffusion encoding along the LR and AP axes. LR: left–right; AP: anterior–posterior; SI, superior–inferior

How to cite this article: Michael ES, Hennel F, Pruessmann KP. Motion-compensated diffusion encoding in multi-shot human brain acquisitions: Insights using high-performance gradients. *Magn Reson Med*. 2024;1-17. doi: 10.1002/mrm.30069